This is the author accepted manuscript of the publication: Kaluthantrige Don, M. A., Feng, J., & Gil-Fernández, J. (2024). Convolutional-neural-network-based autonomous navigation of Hera mission around Didymos. Journal of Guidance, Control and Dynamics, 1-14. https://doi.org/10.2514/1.G008054

Convolutional Neural Network-based autonomous navigation of Hera mission around Didymos

Aurelio Kaluthantrige* and Jinglang Feng†
University of Strathclyde, G1 1XJ, Glasgow, United Kingdom

Jesús Gil-Fernández ‡
ESA, 2201 AZ, Noordwijk

The European Space Agency (ESA)´s Hera mission requires an autonomous visual based navigation in order to safely orbit around the target binary asteroid system Didymos and its moon Dimorphos in 2027. Nevertheless, the performance of optical based navigation systems is depending on the intrinsic properties of the image, such as high Sun phase angles, the presence of other bodies and, especially, the irregular shape of the target. Therefore, to improve the navigation performance, thermal and/or range measurements from additional on-board instruments are usually needed to complement optical measurements. However, this work§ addresses these challenges by developing a fully visual-based autonomous navigation system using a Convolutional Neural Networks (CNN)-based Image Processing (IP) algorithm, and applying it to the Detailed Characterization Phase of the proximity operation of the mission. The images taken by the on-board camera are processed by the CNN-based IP algorithm that estimates the position of the geometrical centers of Didymos and Dimorphos, the range from Didymos and the associated covariances. The results shows that the developed algorithm can be used for a fully visual based navigation for the position of the Hera spacecraft around the target with good robustness and accuracy.

Nomenclature

AE = Absolute Error

$^\circ$ = Degree

ν = Pixel size

ρ = Range

σ = Standard Deviation

*PhD student, Department of Mechanical and Aerospace Engineering, 75 Montrose St; mewantha.kaluthantrige-don@strath.ac.uk.
†Lecturer, Department of Mechanical and Aerospace Engineering, 75 Montrose St; jinglang.feng@strath.ac.uk.
‡Guidance, Navigation and Control Engineer, ESTEC, Keplerlaan 1; jesus.gil.fernandez@esa.int.
§Part of this work was presented at the *2022 AAS/AISS Astrodynamics Specialist Conference*, in Charlotte, North Carolina, in August 2022, Manuscript ID: AAS 22-720

au = Astronomical unit

B = Byte

COM = Center of Mass

d = Days

f = Focal length

h = Hours

m = Meter

P = Covariance matrix of the state

PE = Percent Error

pxl = Pixel

Q = Covariance matrix of the process

R = Covariance matrix of the measurement

s = Seconds

v = Velocity

y = years

I. Introduction

Small celestial bodies are remnants of the ancient Solar System, holding invaluable insights into its evolutionary history. Asteroids and comets have garnered attention as prime targets for numerous space missions in the past years, such as Hayabusa 1 and 2 exploring asteroid Itokawa, Rosetta, a comet rendezvous mission targetting Comet 67P/Churyumov-Gerasimenko, and OSIRIS-REx that sampled asteroid Bennu [1–4]. The European Space Agency (ESA) contributes to small bodies exploration with Hera, a planetary defense mission under development in their Space Safety and Security Program. The Hera mission represents the European contribution to the international collaboration Asteroid Impact and Deflection Assessment (AIDA) with NASA. The main purpose of AIDA is to demonstrate the deflection of a hazardous asteroid by means of kinetic impact. The Double Asteroid Redirection Test (DART) spacecraft is the kinetic impactor designed by NASA, which performed successfully the impact on the 26th of September 2022. The Hera mission will rendezvous in early 2027 with the target asteroid and characterize its physical and dynamical properties, including the crater made by the impactor and the momentum transfer efficiency [5, 6]. Furthermore, Hera aims to bring clarity to the currently uncertain mass measurements of the asteroid and it will delve into the possible presence of recently deposited material, which could potentially constitute reaccreted ejecta following the impact of DART.

The destination of Hera is (65803) Didymos, a binary asteroid consisting of the primary Didymos and its moon

Dimorphos, objective of DART's impact. Table 1 shows the relevant characteristics of the binary asteroid system, provided by the Didymos Reference Model document and updated with the Design Reference Asteroid document that reports data collected with the DART mission [7, 8]. Accompanying Hera on this mission are two CubeSats: Milani and Juventas. While Milani is tasked with capturing detailed imagery of the DART crater, Juventas will conduct comprehensive assessments of Dimorphos' internal structure [9].

Table 1 Didymos' characteristics [7, 8]

Property	**Didymos**	**Dimorphos**
Gravitational parameter $[km^3/s^2]$	$3.5 \cdot 10^{-8}$	$2 \cdot 10^{-10}$
Extent along principal axis x $[m]$	849	177
Extent along principal axis y $[m]$	851	174
Extent along principal axis z $[m]$	620	116

Following the interplanetary cruise phase, Hera will perform a series of Delta-Vs in order to reduce the relative velocity of the spacecraft with respect to the target, which marks the beginning of the proximity operations. The focus of this research is on the Early Characterization Phase (ECP) and the Detailed Characterization Phase (DCP) designed to achieve physical and dynamical characterizations of the binary asteroid [10]. Specifically, the characterization is aimed to improve the accuracy of the values shown in Table 1, together with other parameters related to the binary system, such as the rotation rate of both bodies, the geometric albedo, mass properties and the gravitational field.

To ensure a high level of autonomy the spacecraft is equipped with on-board instruments to accurately determine its position relative to the asteroid system. To meet this requirement, a vision-based navigation system is implemented in the Guidance, Navigation, and Control (GNC) system of the spacecraft, which incorporates an on-board camera, image processing algorithms and a navigation filter. The HERA GNC baseline incorporates a hyperspectral/thermal camera and a laser altimeter called Planet ALTimeter (PALT). These additional instruments enhance the navigation strategy's reliability: the hyperspectral/thermal imager helps to overcome limitations caused by shadows and Sun phase angle issues, while PALT improves estimations in the radial direction, which are typically challenging for a vision-based GNC system. The camera employed in this system is the Asteroid Framing Camera (AFC) [11].

Each day during the proximity operations is divided into two operational segments: data acquisition and data transmission. Within a single operational day, one set of each is scheduled in the following sequence: 15.5 h for acquisition and 8.5 h for transmission. For the ECP and the DCP an autonomous attitude navigation is designed, which relies on an Image Processing (IP) algorithm that estimates the pixel-position of the Center of Mass (COM) of the main body in the images. Subsequently, the algorithm estimates the Line of Sight (LOS) of the spacecraft [11, 12]. During the ECP, the performance of the autonomous attitude navigation system is rehearsed while the spacecraft is flying at a safer distance from the target. Data gathered during the ECP is transmitted to ground within the time interval of data transmission in order to update, if necessary, the IP algorithm. Once the system is verified, the system can be used

during the DCP [13].

Despite the validation process, standard IP algorithms are strongly influenced by the inherent characteristics of the taken images. Elements such as the overall noise, lighting status, the appearance of secondary or undesired objects, and the irregular shape of the target can all impact the accuracy of the optical measurements [14–16]. While the GNC system of the Hera mission tackles these IP challenges by relying on the additional on-board instruments, the authors of this work addressed them with a Convolutional Neural Networks (CNN)-based IP algorithm built and presented in [17]. The algorithm is able to estimate accurately from the images captured by the AFC the position of the centroids of Didymos and Dimorphos and the range from the primary during the ECP and the DCP trajectories. The reader is referred to that work for a comprehensive understanding of the pipeline undertaken for the development of such algorithm. Nevertheless, the work is performed with the pre-impact shape models of Didymos and Dimorphos.

In this work we build upon the CNN-based IP algorithm to develop a fully autonomous visual based navigation algorithm for the DCP trajectory of the Hera mission around the target body Didymos. We leverage the previous phase of the mission, the ECP, to train the CNN-based IP algorithm with a dataset of images representing the new shape of the targets Didymos and Dimorphos. The algorithm is expanded by providing the covariance matrix associated to each measurement and a Flag that inform the filter whether the centroid of Dimorphos is visible or not, which is a unique contribution of this work. An Unscented Kalman Filter (UKF) combines the measurements obtained by the CNN-based IP algorithm with the information retrieved from the dynamical environment to provide the optimal estimate of the relative position of the spacecraft with respect to Didymos. In addition, the developed navigation algorithm relies fully on the AFC without requiring the inputs of the hyperspectral/thermal imager and PALT. Another contribution of this work is the utilization of the position of the centroid of Dimorphos for navigation.

The organization of this paper is as follows. Section II reviews the state of the art of navigation systems around smaller bodies. Section III describes more in detail the proposed IP algorithm and the navigation filter. In Section IV, we conduct the numerical simulations and discuss the results. Section V, in conclusion, summarizes this research and suggests prospective areas for future work.

II. Related methods

This section gives a review on the navigation strategies adopted by previous mission that successfully approached small solar system bodies.

A. Heritage missions

1. Rosetta

In July 2014, the ESA interplanetary spacecraft Rosetta conducted a rendezvous with the comet 67P/Chuyumov-Gerasimenko. At 130 km of distance with respect to the target, Rosetta navigated towards the target relying on optical

measurements provided by the on-board navigation camera NAVCAM. The strategy consisted in matching the newly acquired images with a database of old images for which the geometry is known, using small scale 3D high resolution maps (maplets) built around visible landmarks of the target body. The maplets consist of a height and an albedo map built on-ground with the available shape model of the target [18].

2. Hayabusa 1 and 2

Hayabusa 1 spacecraft performed approaching and landing on the target asteroid Itokawa in November 2005. To maintain the relative position to the asteroid during proximity operations a visual-based GNC system was developed, similar with that of the Hera mission. Two wide-angle cameras, an IP algorithm estimating the position of the centroid of the target and a Light Detecting And Ranging (LIDAR) estimating the range from the target have been used.

Hayabusa 2 spacecraft approached the target asteroid Ryugu in July 2018. As its predecessor Hayabusa 1, this spacecraft is also provided with two wide-angle cameras and a LIDAR. Both spacecraft had on board a Thermal Infrared Imager and a Near-Infrared Camera Spectrometer for scientific purposes but also to increase the robustness of the navigation system as for the Hera mission [19, 20].

3. OSIRIS-REx

OSIRIS-REx used two wide-range cameras of the camera suite OCAMS and the touch-and-go camera system TAGCAMS for the proximity operations navigation around the target asteroid Bennu. Stereophotoclinometry was used to create digital terrain maps for landmark tracking technique, while the on-board LIDAR solves for the radial direction estimation [21].

4. DART

DART utilized the Small-body Maneuvering Autonomous Real-Time Navigation (SMART Nav) algorithm in conjunction with images obtained from the on-board Didymos Reconnaissance and Asteroid Camera for Optical navigation (DRACO) to carry out autonomous terminal navigation in order to target the center of brightness (COB) of Dimorphos. The on-board ephemeris was updated with optical navigation data collected by DRACO till about 4 hours before the impact, after which the spacecraft went fully autonomous with SMART Nav [22].

B. Summary

The navigation techniques involved in Rosetta and OSIRIS-REx have in common the usage of asteroid models to be rendered for correlation with real images acquired with the on-board cameras. Therefore, prior knowledge of the surface appearance of Didymos would be required to employ these navigation strategies. Furthermore, the more complex is the model, the more computationally expensive is to run the technique on-board. To apply DART' SMART Nav algorithm, constant direct communication with ground is necessary for the real-time updating of the ephemeris, which is not the

This is the author accepted manuscript of the publication: Kaluthantrige Don, M. A., Feng, J., & Gil-Fernández, J. (2024). Convolutional-neural-network-based autonomous navigation of Hera mission around Didymos. Journal of Guidance, Control and Dynamics, 1-14. https://doi.org/10.2514/1.G008054

case of Hera that alternates its attitude for data acquisition and transmission. Finally, the optical navigation solutions employed by Hayabusa 1 and 2 are similar to Hera and as such rely on multiple instruments to improve the robustness, while the purpose of this work is to provide a navigation strategy with good robustness that relies only the images captured by the on-board camera.

III. Methodology

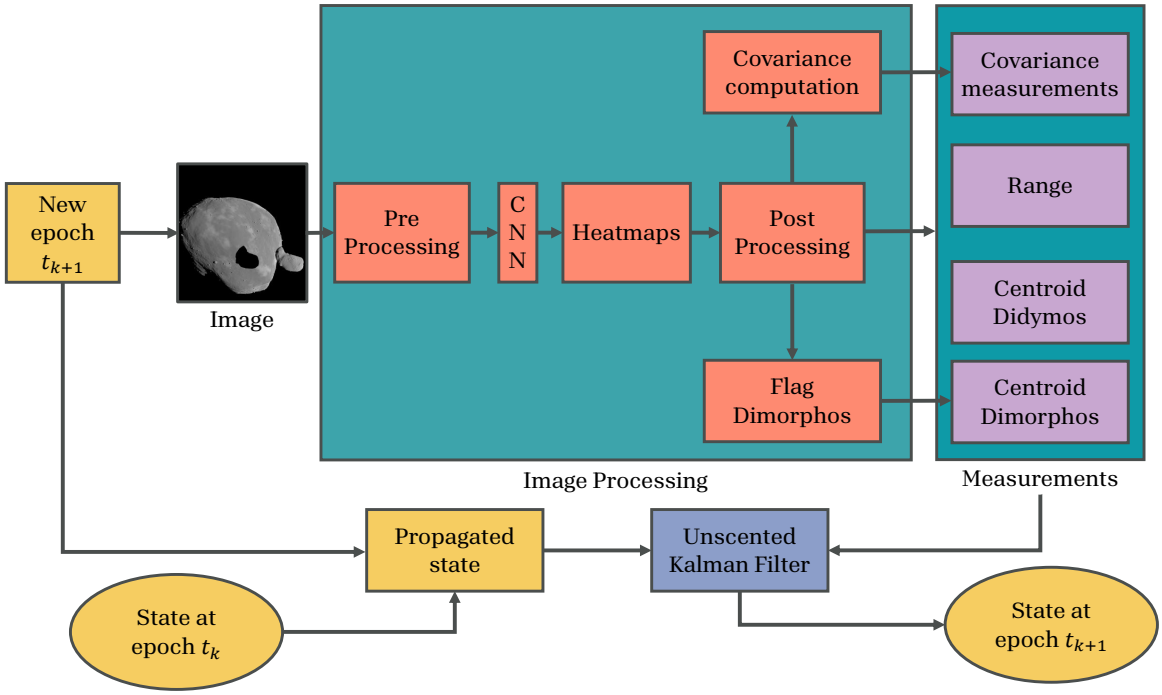

Fig. 1 Overall visual based navigation algorithm

This section provides a detailed description of the methodology applied in this work. A terminology is briefly clarified to streamline the discussion. In this work, with centroid or Center of Mass (COM) is intended as the body's geometrical center projected on the image. While this assumption is almost valid for Didymos given its ellipsoidal shape, it is not certain if it holds true for Dimorphos consequently to the DART impact that may have modified its shape [23]. Fig. 1 shows the main steps of the overall pipeline. Given a reference trajectory, at epoch t_{k+1} a new image is captured by the on-board AFC. In this work, synthetic images generated with the software Planet and Asteroid Natural scene Generation Utility (PANGU) are used. The image is input to the IP block and it goes several steps detailed in Section III.C in order to provide 4 different estimations: the position of the centroid of Didymos, the range from Didymos, the centroid of Dimorphos (if available), and the associated covariance matrix for each measurement. The IP consists firstly in a Pre-Processing step where the image undergoes an initial normalization before it is handled by the CNN aimed to regress specific keypoints on the image. The CNN outputs a sequence of heatmaps, each one associated

with the regressed keypoint. The Post-Processing block analyzes the heatmaps and outputs the position of the keypoints and the intensities of the heatmaps. The latter are used to calculate the covariance matrices and to inform whether an estimate of Dimorphos' centroid position is available with a boolean variable represented by Flag Dimorphos. Finally, an Unscented Kalman Filter (UKF) combines the available measurements and the propagated state to provide the best estimate for the state of the spacecraft at epoch t_{k+1}.

This work is an extension of [17], where the main focus was to build an IP algorithm supported by CNNs able to provide optical measurements for the navigation of Hera using the pre-impact shape models of Didymos and Dimorphos. In contrast, this research is focused on refining the previous algorithm with the latest shape models, and combining it with an UKF in order to solve for the state estimation of the Hera spacecraft. We use the same reference trajectories (Section III.A), software to generate the database of images (Section III.B), CNN architecture (Section III.C.2) and centroiding and range estimation methodologies (Section III.D). The subsequent part of this section contains a thorough explanation of the applied methodology.

A. Reference trajectories

The reference trajectories used in this work are represented in the Target Body Equatorial Inertial (TB) reference frame, which has the geometrical center of Didymos as origin of the axes, the X-axis pointing as the Earth-Centered Ecliptic Inertial, and the XY plane lying in the same plane as the equator of Didymos. A summary of the most relevant information of the orbit of the binary system is reported in Table 2 [24, 25]. The orbit of Dimorphos considered in this work is prior to the DART impact. The reference trajectories employed in this work are from the ECP and the DCP proximity operations. The former is used to train the CNN and to tune the parameters of the Post-Processing, while the latter is used as a test case scenario.

Table 2 Selected orbital properties of Didymos system [24, 25]

Heliocentric orbit	
Semi-major axis $[au]$	$1.642665 \pm 2.7214e-9$
Eccentricity []	$0.383264 \pm 1.3374e-10$
Inclination $[^\circ]$	$3.41415 \pm 1.6188e-8$
Longitude of ascending node $[^\circ]$	$72.987867 \pm 2.1852e-7$
Orbital period $[y]$	$2.105386 \pm 5.2320e-10$
Binary orbit	
Semi-major axis $[m]$	1190 ± 30
Eccentricity []	0
Orbital period $[h]$	11.93 ± 0.01

The ECP trajectory is provided by ESA while the DCP trajectory is provided by GMV Aerospace and Defence, in charge of the GNC simulator of the Hera mission. Both trajectories consist of hyperbolic arcs: the spacecraft cannot

This is the author accepted manuscript of the publication: Kaluthantrige Don, M. A., Feng, J., & Gil-Fernández, J. (2024). Convolutional-neural-network-based autonomous navigation of Hera mission around Didymos. Journal of Guidance, Control and Dynamics, 1-14. https://doi.org/10.2514/1.G008054

be placed into captured orbits due to the limited prior knowledge of Didymos' dynamical environment. The arcs are designed so that the AFC, whose parameters are shown in Table 3, is able to contain within its Field Of View (FOV) the whole shape of Didymos in a single image in order to use the centroiding algorithm [13, 26, 27].

Table 3 AFC properties [26, 27]

FOV	**Focal length**: f	**Aperture**	**Image size**	**Pixel size**: ν
5.5°	10.6 cm	2.5 cm	1024 X 1024 pxl	14 μm

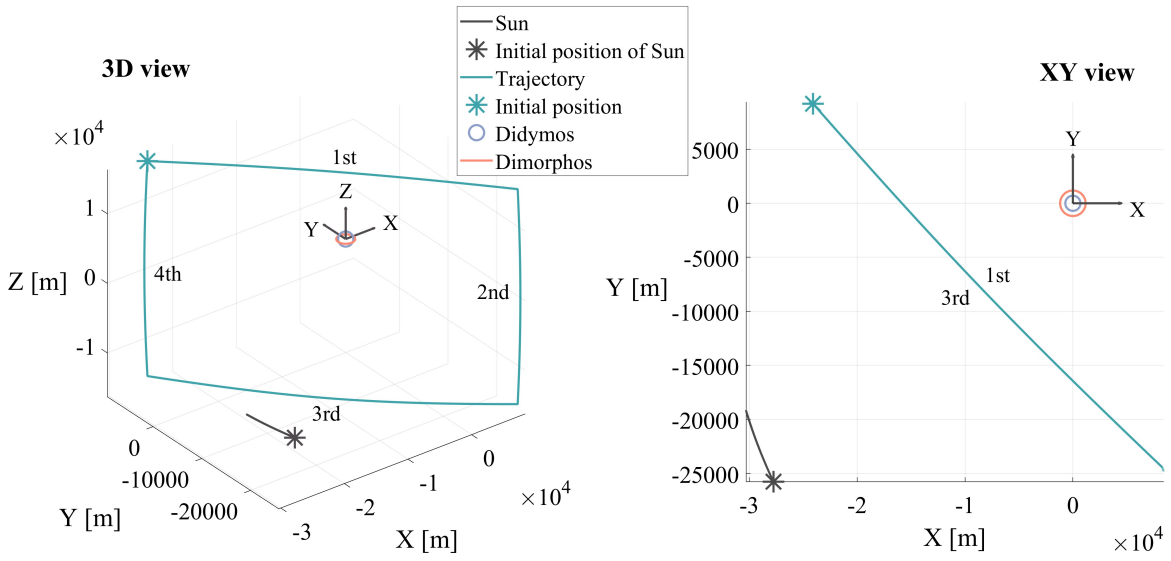

Fig. 2 ECP trajectory

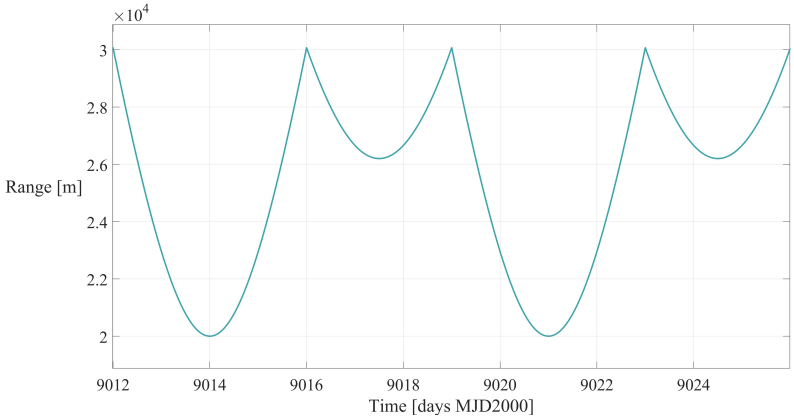

Fig. 3 Range from Didymos during ECP trajectory

Fig. 2 depicts the spacecraft's ECP trajectory along with the relative position of the Sun (reduced in size in the visual representation) and Dimorphos' orbit. The trajectory is composed of four arcs, with the initial epoch set at t_{in} = 9012 d

This is the author accepted manuscript of the publication: Kaluthantrige Don, M. A., Feng, J., & Gil-Fernández, J. (2024). Convolutional-neural-network-based autonomous navigation of Hera mission around Didymos. Journal of Guidance, Control and Dynamics, 1-14. https://doi.org/10.2514/1.G008054

and the final epoch at t_{fin} = 9026 d calculated in the Modified Julian Date 2000 (MJD2000). The 2^{nd} and the 4^{th} arcs are 3 d long and go respectively from Didymos' high latitudes to low latitudes and viceversa. The 1^{st} and the 3^{rd} arcs are 4 d long and cover the poles of the target. The sole gravitational forces from the point masses of both bodies and the orbital manoeuvres at the joint of two arcs are taken into account. The planar view illustrated in Fig. 2 shows that the ECP trajectory is placed between the Sun and Didymos in order to provide the AFC with visible images of the target [10]. Fig. 3 shows that the distance from the primary ranges from 20 km and to 30 km.

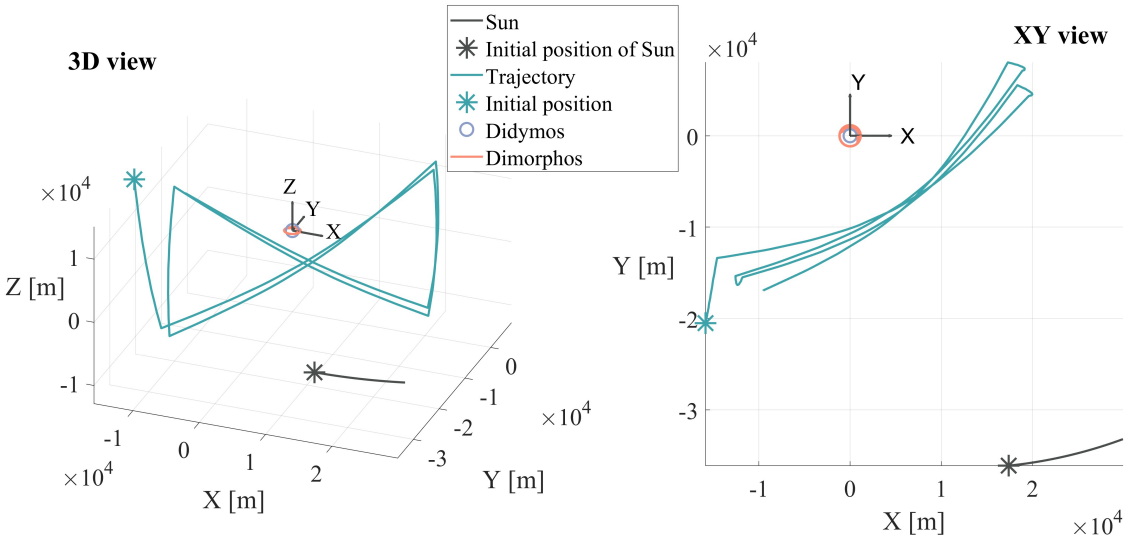

Fig. 4 DCP trajectory

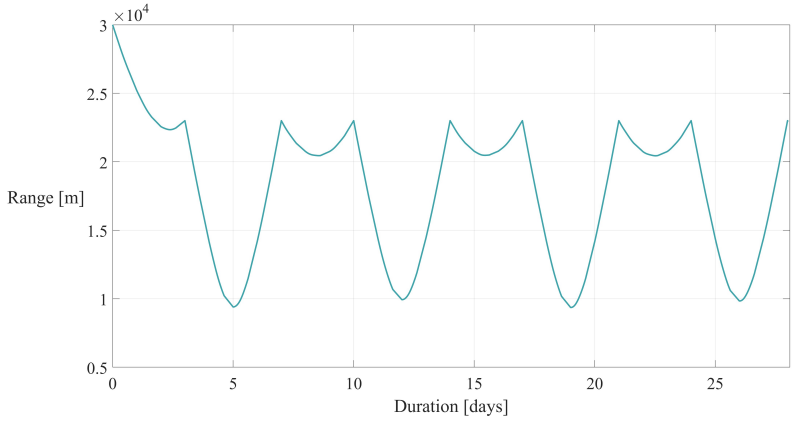

Fig. 5 Range from Didymos during DCP trajectory

Fig. 4 depicts the spacecraft's DCP trajectory along with the relative position of the Sun (reduced in size in the visual representation) and Dimorphos' orbit. The trajectory is composed of eight Z-shaped arcs located between the target and the Sun's position, with a total duration of 28 d, plus 3 d of transition from the ECP. The distance from the

This is the author accepted manuscript of the publication: Kaluthantrige Don, M. A., Feng, J., & Gil-Fernández, J. (2024). Convolutional-neural-network-based autonomous navigation of Hera mission around Didymos. Journal of Guidance, Control and Dynamics, 1-14. https://doi.org/10.2514/1.G008054

primary ranges approximately from 9 km to 23 km, as illustrated in Fig. 5. The minimum distance is established to guarantee that the complete shape of Didymos remains within the FOV of the AFC, even when there is a navigation error of up to 100 m. In the actual mission, the ECP and the DCP last 4 weeks each but in this work the whole DCP and only half of the ECP are considered, as provided by ESA and GMV Aerospace and Defence.

B. Image Generation

The software PANGU is used to generate the database of synthetic images for this work. PANGU is a simulation tool developed by the STAR-Dundee engineering company, and it is capable of modeling planetary and asteroid surfaces and providing high-fidelity visualizations of images in near real-time [28]. The shape models of Didymos and Dimorphos are provided by GMV and updated with the data collected with the DART mission shown in Table 1. Didymos' shape is ellipsoidal, with the extent along its x- and y-axes larger than the extent along its z axis, as shown in Table 1. Dimorphos' shape prior to DART's impact was an oblate ellipsoid, which is approximated in this work scaling down the shape model of asteroid Itokawa.

PANGU generates grayscale images as seen from the AFC with the properties shown in Table 3, and displays them on its viewer with its coordinate frame's origin at the top left corner and the horizontal and vertical axes referred to as i-direction and j-direction, respectively, as illustrated in the example of Fig. 6.

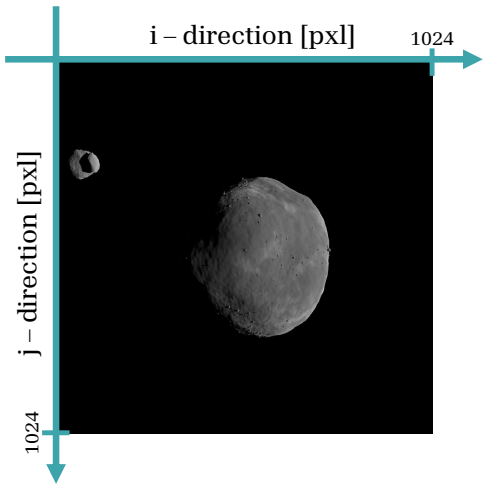

Fig. 6 Image taken during the ECP trajectory shown on the PANGU viewer

For asteroid imaging during the ECP and DCP trajectories, the AFC's boresight is aligned with Didymos' position vector, and the camera's vertical axis is orthogonal to the spacecraft-Sun's position vector to the spacecraft [10], which results on images displayed on the viewer consistently portraying the target illuminated from the right side.

In this work, PANGU is used to generate:

This is the author accepted manuscript of the publication: Kaluthantrige Don, M. A., Feng, J., & Gil-Fernández, J. (2024). Convolutional-neural-network-based autonomous navigation of Hera mission around Didymos. Journal of Guidance, Control and Dynamics, 1-14. https://doi.org/10.2514/1.G008054

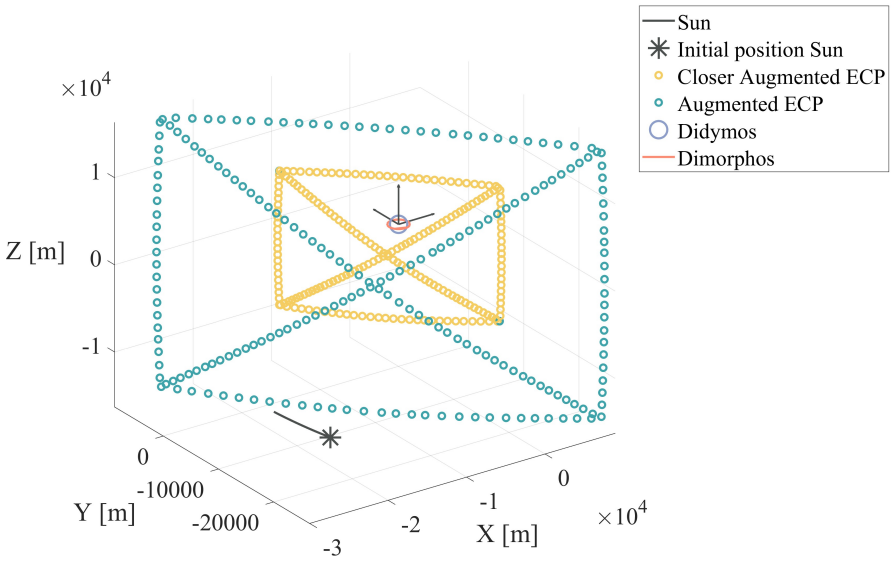

Fig. 7 Augmented ECP trajectory

- Dataset 1: $40,000$ images generated during the ECP trajectory and used for the training and validation of the CNN and to tune the parameters of the IP algorithm. Two fictitious additional arcs are considered, the first arc connecting the end of the 2^{nd} arc with the beginning of the 1^{st} one, and the second one connecting the end of the 3^{rd} arc with the end of the 1^{st} one, as shown in Fig. 7. The augmented ECP trajectory is sampled randomly to generate a secondary trajectory closer to the target, with a minimum distance of 7 km, in order to train and validate the IP algorithm with a pool of images showing the asteroid in multiple configurations relative to the spacecraft. A pointing error of the AFC boresight direction with values spanning between $[-0.3, 0.3]^\circ$ is considered for each image to randomize the position of the projected centroid of Didymos on the image plane;
- Dataset 2: 450 images taken sampling the DCP trajectory every 3600 s and used as testing batch for the whole visual based navigation pipeline. A pointing error of the AFC boresight direction with values spanning between $[-0.5, 0.5]^\circ$ is considered for each image to randomize the position of the projected centroid of Didymos on the image plane.

The pointing error values considered in the generation of the images of Dataset 1 and Dataset 2 are chosen taking into account the only mission requirement of having the whole shape of Didymos within the FOV of the camera [10].

C. Image Processing

In this section the operations that each image undergoes with the IP algorithm are described, as represented in Fig. 8.

This is the author accepted manuscript of the publication: Kaluthantrige Don, M. A., Feng, J., & Gil-Fernández, J. (2024). Convolutional-neural-network-based autonomous navigation of Hera mission around Didymos. Journal of Guidance, Control and Dynamics, 1-14. https://doi.org/10.2514/1.G008054

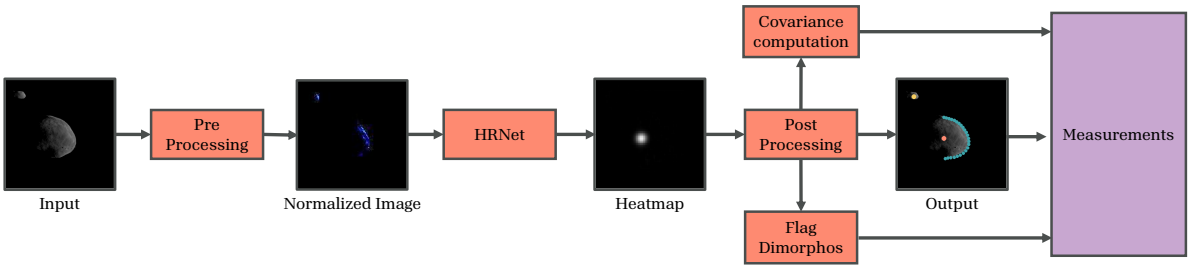

Fig. 8 Image Processing

1. Normalization

Once an image is generated with PANGU, its size is reduced from 1024 X 1024 *pxl* to 256 X 256 *pxl* and consequently it is normalized using Eq. 1 to calibrate the different pixels intensities, which helps the CNN to converge faster for a given learning rate. Eq. 1 shows that the image is converted from grayscale to RGB as required from the specific CNN architecture chosen in this work.

$$Image = Image - Mean/std \tag{1}$$

where $Mean = [0.485, 0.456, 0.406]$ and $Std = [0.229, 0.224, 0.225]$. Fig. 8 shows the output normalized image of the Pre-Processing block (the colors of the output image are enhanced for visualization purposes).

2. CNN

The CNN employed in this work is the High-Resolution Network (HRNet), the state-of-the-art CNN architecture for keypoints regression, with its ability to maintain high resolution representation of the input image through the whole net [29]. The keypoints to regress for each synthetic image are 26, and they are the COM of Didymos, COM_{Did}, the COM of Dimorphos, COM_{Dim}, and 24 points on the visible limb, i.e. the right side, segmenting Didymos from the background. The positions of the 24 points are used together with the position of the COM_{Did} to estimate the range from Didymos, as it is explained in Section III.D. The reader is referred to [17] for the methodology applied to retrieve the Ground Truth (GT) positions of the 26 keypoints on the images.

In this work, we utilize the CNN architecture known as pose-hrnet-w32 [30]. Throughout the training process, the validation dataset is employed alongside the training dataset to calculate validation losses, thereby preventing overfitting. For the training and validation Dataset 1 is not used entirely, as images where Dimorphos is located outside of the image plane or behind Didymos are discarded. Whether Dimorphos is visible or not in the testing Dataset is handled by the Post-Processing block of the IP. Consequently, the training and validation datasets consist respectively of 15, 156 (93.73%) images and 520 (3.22%) images from Dataset 1, while the testing dataset consists of the whole 450 (3.05%)

This is the author accepted manuscript of the publication: Kaluthantrige Don, M. A., Feng, J., & Gil-Fernández, J. (2024). Convolutional-neural-network-based autonomous navigation of Hera mission around Didymos. Journal of Guidance, Control and Dynamics, 1-14. https://doi.org/10.2514/1.G008054

images from Dataset 2. The training utilizes the Adam optimizer, employing a learning rate that follows a cosine decay schedule, initialized at 10^{-3} and decaying at a rate of 0.1. The overall number of parameters engaged in the training process amounts to $28,536,410$.

The CNN model undergoes training for 210 epochs, which approximately equates to 48 h of training time. This training is conducted on a virtual machine hosted by Google Colab, utilizing the NVIDIA V100 Tensor Core GPU. The trained model is then converted into an *ONNX* (Open Neural Network Exchange) open format and imported on Matlab. The trained HRNet with the updated weights and biases has an overall weight of 109 MB.

The outputs of the HRNet consist in a sequence of heatmaps of size 64 X 64 pxl, each one associated with the corresponding keypoint. A heatmap is a cloud of white pixels around the estimated keypoint, and it represents the estimated accuracy in regressing the position of that particular keypoint. The smaller and intense is the heatmap, the more accurate is the estimation of the position of the associated keypoint. Fig. 9 shows an example of the heatmap around the estimated position of the COM of Didymos.

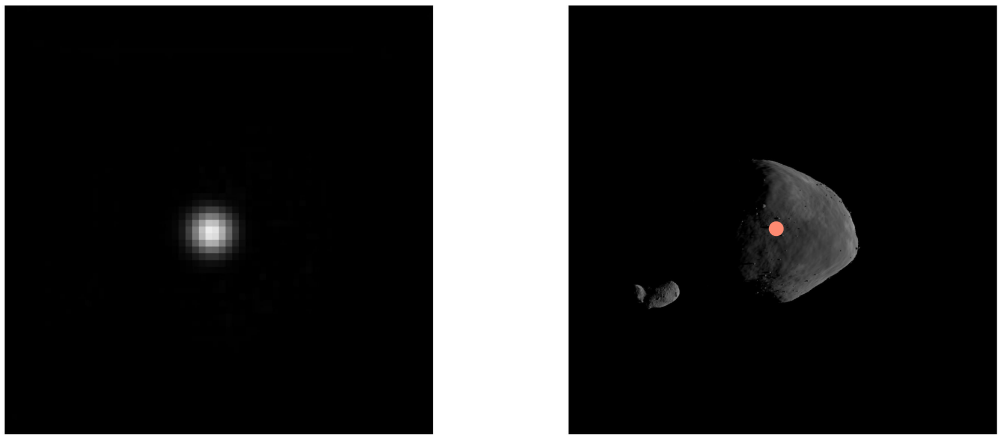

Fig. 9 Heatmap associated to the position of the centroid of Didymos

3. Post-Processing

In the Post-Processing block, the 26 heatmaps associated to each keypoint are analyzed. Specifically, the Post-Processing block has three main functions:

- ❖ To remove the white noise by thresholding each heatmap image so that the only non-black pixels are the one associated to the heatmap;
- ❖ To extract the peak intensity of the heatmap and its x and y coordinates;
- ❖ To obtain a statistical population around the heatmap's peak.

The coordinates of the points with the peak pixel intensity within the heatmap defines the estimated position of the regressed 26 keypoints. The intensity and shape of the heatmap conveys the level of confidence in accurately pinpointing

This is the author accepted manuscript of the publication: Kaluthantrige Don, M. A., Feng, J., & Gil-Fernández, J. (2024). Convolutional-neural-network-based autonomous navigation of Hera mission around Didymos. Journal of Guidance, Control and Dynamics, 1-14. https://doi.org/10.2514/1.G008054

the associated keypoint at that particular position. Therefore, in this work the statistical population around the regressed keypoint is used to derive the associated covariance matrix.

4. Flag Dimorphos

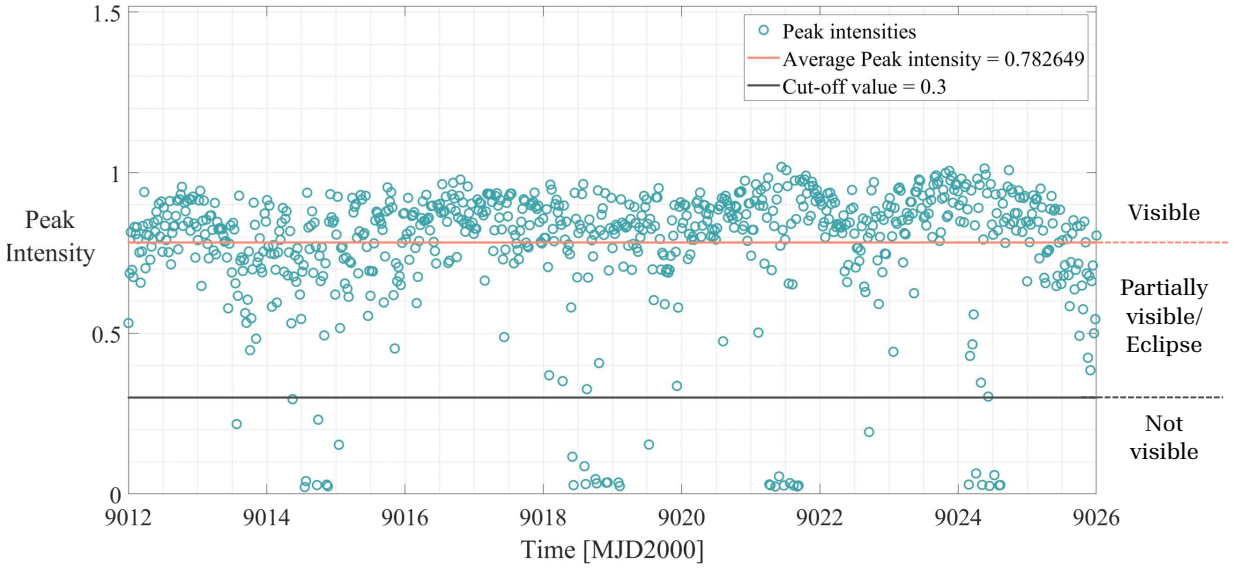

Fig. 10 Peak intensity of the heatmaps associated to COM_{Dim} generated with Dataset 1

By analyzing the peak intensity of the heatmaps associated to the COM of Dimorphos and generated by the trained HRNet with the entire Dataset 1, it is derived a threshold value to determine whether Dimorphos is visible or not. Fig. 10 shows the mentioned peak intensities, together with their average value and the cut-off threshold value. Three main regions of peak intensities are identified:

- 0 - 0.3: Heatmaps peak intensities associated to images where Dimorphos is hardly visible or not visible;
- 0.3 - 0.782649: Heatmaps peak intensities associated to images where Dimorphos is in eclipse or is partially visible;
- > 0.782649: Heatmaps peak intensities associated to images where Dimorphos is fully visible.

Fig. 11 shows three sample images of each region along with the heatmaps associated with the regression of the centroids of both bodies. The output of this block is a boolean variable that is true if the peak intensity of Dimorphos' centroid heatmap is higher than 0.3, i.e. Dimorphos is at least partially visible or in eclipse.

This is the author accepted manuscript of the publication: Kaluthantrige Don, M. A., Feng, J., & Gil-Fernández, J. (2024). Convolutional-neural-network-based autonomous navigation of Hera mission around Didymos. Journal of Guidance, Control and Dynamics, 1-14. https://doi.org/10.2514/1.G008054

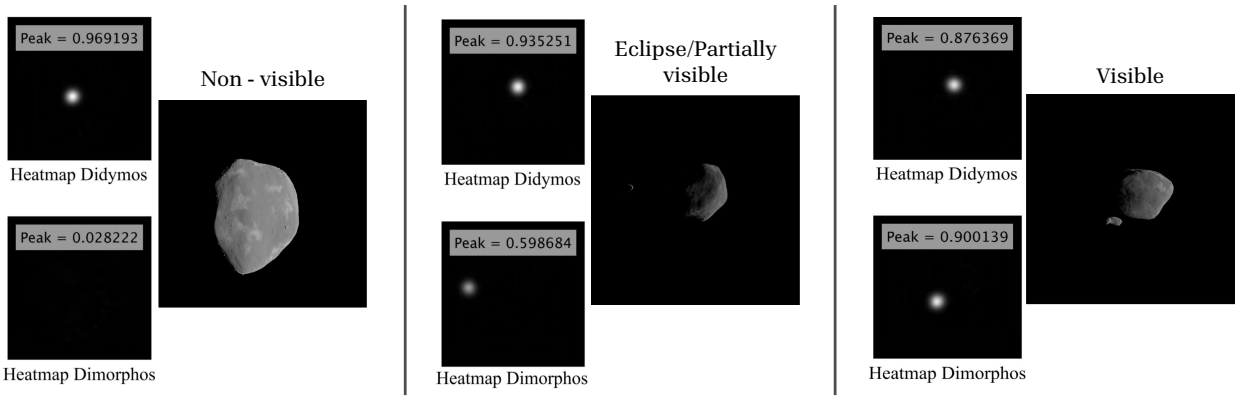

Fig. 11 Heatmaps of COM_{Did} and COM_{Dim} associated with three sample images showing Dimorphos respectively non-visible, in eclipse and visible

5. Covariance computation

In this block of the IP algorithm, the covariance matrices associated to the error in the estimation of the position of the centroids of Didymos and Dimorphos are computed. Given the x_i- and y_i- coordinates of the $i-$th pixel belonging to the heatmap associated to the regressed centroid of coordinates x_p and y_p, the covariance of the error is calculated with Eq. 2 and Eq. 3, in accordance with [31].

$$P_{COM} = \begin{pmatrix} cov(x,x) & cov(x,y) \\ cov(y,x) & cov(y,y) \end{pmatrix} \tag{2}$$

$$cov(x,y) = \sum_{i=1}^{n} w_i (x_i - x_p) \cdot (y_i - y_p) \tag{3}$$

where n is the number of pixels in each keypoint's heatmap and w_i is a weight that takes into account the intensity of the pixel belonging to the heatmap. This process aims to assign greater weight to pixels that exhibit high brightness and are situated near the peak, while assigning reduced importance to pixels with low intensity that are distant from the peak. Fig. 12 shows two examples of covariance matrices associated to the estimation of the centroids of both bodies. The example on the image of the right of Fig. 12 shows that Dimorphos' centroid estimation covariance can reach lower values than the one of Didymos due to its relative reduced size on the image. Therefore, the cloud of points associated to Dimorphos' centroid estimation is smaller. In order to account for the different size of the bodies, a tuning of the covariance is applied accordingly. The tuning consists in adjusting the parameters of the covariance matrices to weigh majorly the estimation of the centroid of Didymos with respect to the one of Dimorphos.

This is the author accepted manuscript of the publication: Kaluthantrige Don, M. A., Feng, J., & Gil-Fernández, J. (2024). Convolutional-neural-network-based autonomous navigation of Hera mission around Didymos. Journal of Guidance, Control and Dynamics, 1-14. https://doi.org/10.2514/1.G008054

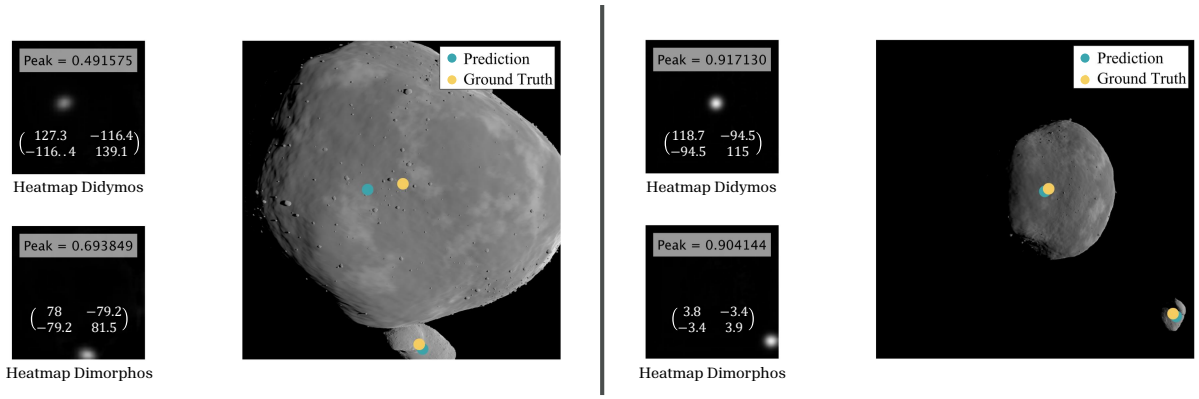

Fig. 12 Two example of covariance matrices associated to the centroids of Didymos and Dimorphos

D. Measurements

The input measurements of the navigation filter are the estimated position of the centroids of Didymos and Dimorphos (when available) and the estimated range from Didymos. The first two are direct outputs of the IP block together with their associated covariance matrices. The range is estimated using the relative average distance in pixel (n_R) of the 24 regressed keypoints on the visible limb of Didymos with respect to its estimated COM, as explained in [17]. The 24 keypoints have an equal relative angular distance and span an angular aperture of $[-87, 87]^\circ$ with respect to the $i-$direction of the PANGU viewer. By applying the pinhole camera model using the properties of the AFC shown in Table 3, and by approximating the shape of Didymos as a sphere of radius $R = 773.33\ m$ (average value of the extent along the three principal axis shown in Table 1), the range ρ is estimated, as shown in Eq. 4:

$$\rho = \frac{f \cdot R}{n_R \cdot \nu} \tag{4}$$

where f is the focal length and ν is the pixel density, as shown in Table 3. The covariance of the error associated with the estimated range is obtained by applying Eq. 4 to Dataset 1 and by comparing it with the range's GT value. The error obtained is reported on Table 4 and the covariance of the error chosen in this work is $P\rho = MAE^2$.

Table 4 Range estimation error for Dataset 1

Mean Absolute Error (MAE) $[m]$	854.9
σ_{MAE} $[m]$	518.85
Mean Absolute Percent Error (MAPE) [%]	5.68
σ_{MRAE} [%]	4.3

The Absolute Error (AE) and the Absolute Percent Error (APE) are defined as follows:

$$AE = |Range_{est} - Range_{GT}|, \tag{5}$$

$$APE = \frac{|Range_{est} - Range_{GT}|}{Range_{GT}} \cdot 100\% \tag{6}$$

E. Navigation filter

To combine the measurements produced by the image processing algorithm with the dynamical environment and form an accurate estimate of the state of the spacecraft, a navigation filter is implemented. The relative state of the spacecraft with respect to Didymos to be estimated consist of the three coordinates of the relative position and the three coordinates of the relative velocity. The measurements are available for each image of Dataset 2, therefore every 3600 s.

The UKF is based on a non-linear uncertainty propagation technique called the Unscented Transform (UT) that captures the propagation of the statistical properties of state estimates through non-linear functions. This is done using a set of sigma points that are built with the matrix square root of the covariance matrix of the state. Assume the following n-state discrete-time non-linear system x with measurement equation z [32]:

$$\begin{aligned} x_{k+1} &= f(x_k) + w_k, \\ z_k &= h(x_k) + v_k, \\ w_k &\sim (0, Q_k), \\ v_k &\sim (0, R_k) \end{aligned}$$

where f is a non-linear state transition function from discrete time k to $k+1$, and w and v are respectively the process and measurement noise. The individual steps of the UKF are shown in Algorithm 1. W_n^i and W_c^i are weights that determines the spread and the distribution of the sigma points around the mean state value, while c is a scaling factor based on the size of the state.

Algorithm 1 The Unscented Kalman Filter

Initialize:

$\hat{x}_0 = \mathbb{E}[x_0]$

$P_0 = \mathbb{E}[(x_0 - \hat{x}_0) \cdot (x_0 - \hat{x}_0)^T]$

for Each measurement z_k at epoch $k = 1, \ldots, t_f$ **do**

Calculate sigma points and the associated predicted measurements:

$\hat{x}^{(0)}_{k|k-1} = \hat{x}_{k|k-1}$

$\Delta x^{(i)} = (\sqrt{cP_{k|k-1}})_i$ for $i = 1, \ldots, n$

$\Delta x^{(n+i)} = -(\sqrt{cP_{k|k-1}})_i$ for $i = 1, \ldots, n$

$\hat{x}^{(i)}_{k|k-1} = \hat{x}_{k|k-1} + \Delta x^{(i)}$ for $i = 1, \ldots, 2n$

$\hat{z}^{(i)}_{k|k-1} = h(\hat{x}^{(i)}_{k|k-1})$ for $i = 1, \ldots, 2n$

Combine the predicted measurements of each sigma point to obtain the mean predicted measurement at time k:

$\hat{z}_k = \sum_{i=0}^{2n} W_n^{(i)} \hat{y}^i_{k|k-1}$

Estimate the covariance of the predicted measurement:

$P_{zz} = \sum_{i=0}^{2n} W_c^{(i)} (\hat{z}^{(i)}_{k|k-1} - \hat{z}_k) \cdot (\hat{z}^{(i)}_{k|k-1} - \hat{z}_k)^T + R_k$

Estimate the cross-covariance:

$P_{xz} = \sum_{i=0}^{2n} W_c^{(i)} (\hat{x}^{(i)}_{k|k-1} - \hat{x}_{k|k-1}) \cdot (\hat{z}^{(i)}_{k|k-1} - \hat{z}_k)^T$

Update Step:

$K_k = P_{xz} P_{zz}^{-1}$

$\hat{x}_{k|k} = \hat{x}_{k|k-1} + K(z_k - \hat{z_k})$

$P_{k|k} = P_{k|k-1} - K_k P_{zz} K_k^T$

Prediction Step:

Calculate the sigma points and propagate with function f:

$\hat{x}^{(i)}_{k|k+1} = f(\hat{x}^{(i)}_{k|k})$

Combine the predicted state for each sigma point to compute the mean predicted state at epoch $k + 1$:

$\hat{x}_{k+1|k} = \sum_{i=0}^{2n} W_n^{(i)} \hat{x}^i_{k+1|k}$

Compute the covariance of the predicted state at epoch $k + 1$:

$P_{k+1|k} = \sum_{i=0}^{2n} W_c^{(i)} (\hat{x}^{(i)}_{k+1|k} - \hat{x}_{k+1|k}) \cdot (\hat{x}^{(i)}_{k+1|k} - \hat{x}_{k+1|k})^T + Q_k$

end for

1. Dynamics and measurement equations

There are various options in terms of modelling the dynamics of the spacecraft. The main forces acting on the spacecraft are the gravitational forces from both Didymos and Dimorphos, the solar radiation pressure (SRP), and the third body gravitation of the Sun. To reduce the computational complexity, the main forces considered in this work are the gravitational attraction of the two bodies of the binary system, as shown in Eq. 7, where the subscripts D and d refer to Didymos and Dimorphos respectively. At the distance of the DCP, it was found that for accurate modelling the point mass model is sufficient [33]. The maneuvers to change the arcs of the DCP are not added into the dynamics, as the measurements are expected to capture these as well.

$$f = -\frac{\mu_D \vec{r_D}}{r_D^3} - \frac{\mu_d \vec{r_d}}{r_d^3} \tag{7}$$

The equations of motion of the spacecraft in the TB reference frame is given as follows.

$$\ddot{\vec{r_H}} = \frac{-\mu_D \vec{r_H}}{\vec{r_H}^3} + \mu_d \left(\frac{-\vec{r_{Hd}}}{\vec{r_{Hd}}^3} - \frac{\vec{r_d}}{\vec{r_d}^3} \right) \tag{8}$$

where $\vec{r_H}$, $\vec{r_{Hd}}$ and $\vec{r_d}$ denote respectively the position vector of the spacecraft with respect to Didymos, the position vector of the spacecraft with respect to Dimorphos, and the position vector of Dimorphos with respect to Didymos, while μ_D and μ_d are the standard gravitational parameters of Didymos and Dimorphos.

The measurement equation correlated with the centroids' estimations is given by the pinhole camera model, which relates the three coordinates of the position x_{COM} of the COM in the TB with its two projected coordinates z_{COM} on the image plane, as shown in Eq. 9 [34].

$$z_{COM} = K[A|t]x_{COM} \tag{9}$$

where K is the calibration matrix that depends on the intrinsic properties of the AFC and A and t are respectively the rotation matrix and the translation vector from TB to the camera reference frame. The rotation matrix A at each point in time is assumed to be given by the on-board attitude determination system.

The range measurement equation is the norm of the spacecraft position vector given in Eq. 10.

$$z_\rho = \sqrt{x^2 + y^2 + z^2} \tag{10}$$

Eq. 9 and Eq. 10 show that both measurements involve the position estimation, which means that the velocity estimation is provided just by the dynamic equation given by Eq. 7. It can also be seen that in the camera reference frame Eq. 9 affects the X and Y coordinates of the position estimation while Eq. 10 affects the Z coordinate.

This is the author accepted manuscript of the publication: Kaluthantrige Don, M. A., Feng, J., & Gil-Fernández, J. (2024). Convolutional-neural-network-based autonomous navigation of Hera mission around Didymos. Journal of Guidance, Control and Dynamics, 1-14. https://doi.org/10.2514/1.G008054

IV. Results

In this section, the results of the visual based navigation algorithm for the relative state estimation of Hera with respect to Didymos during the DCP trajectory are presented. The performances of the IP on estimating the position of COM_{Did} and COM_{Dim} are presented with the absolute error with respect to the GT value, using the metric defined in Eq. 11. This metric is applied to both $i-$ and $j-$ directions of the PANGU viewer. The analysis is conducted only for the absolute error, as the presence of potential systematic error and biases towards positive or negative values of the centroiding estimation error has already been analyzed in [17].

$$\epsilon_{COM} = |COM_{GT} - COM_{est}| \tag{11}$$

These results are compared with the ones shown in Table 5, presented in [17] and obtained applying the same CNN-based IP algorithm on 6052 images generated with PANGU during the ECP trajectory and showing the shape models of Didymos and Dimorphos prior to DART's close encounter. The results shown in Table 5 comply with pointing accuracy requirements of the mission [11].

Table 5 Centroiding results on old shape models of Didymos and Dimorphos [17]

Image axis	ϵ_{COM} **Didymos** $[pxl]$	ϵ_{COM} **Dimorphos** $[pxl]$
i-direction	5.35	11.05
j-direction	4.41	7.17

Fig. 13 shows two sample images of Dataset 2 processed by the HRNet for the 26 keypoints regression.

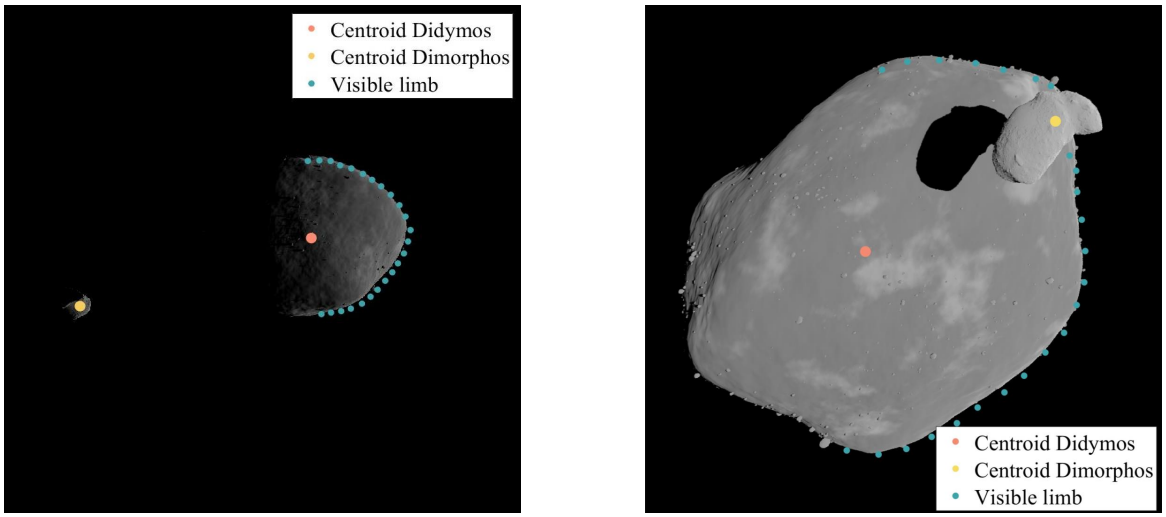

Fig. 13 Two sample images of Dataset 2 with the estimated keypoints

The accuracy on estimating the spacecraft's range from the primary is assessed through the APE with respect to the

This is the author accepted manuscript of the publication: Kaluthantrige Don, M. A., Feng, J., & Gil-Fernández, J. (2024). Convolutional-neural-network-based autonomous navigation of Hera mission around Didymos. Journal of Guidance, Control and Dynamics, 1-14. https://doi.org/10.2514/1.G008054

GT value. The Hera mission requires that the MAPE on the range estimation is lower than 10% along the trajectory [10]. For the ECP, the MAPE obtained by the IP algorithm developed in this work is 2.1385%, thus satisfying the mission requirements. Finally, the results of the navigation filter on the estimated state of the DCP are presented.

The trained model is run with Matlab on the NVIDIA GeForce RTX 2070 with Max Q-design GPU of the local machine. The average computational time required for processing a single image from the IP block is 2.4828 s with a standard deviation of 0.21 s. On an on-board spacecraft-like CPU processor such as the Zynq 7000 System-on-a-Chip, the average computational time is 165 s with a standard deviation of 0.15 s. On a CPU processor with higher performances such as the LEON3 on-board the Hera spacecraft, half the computational time to process a single image is expected.

A. Centroiding Didymos

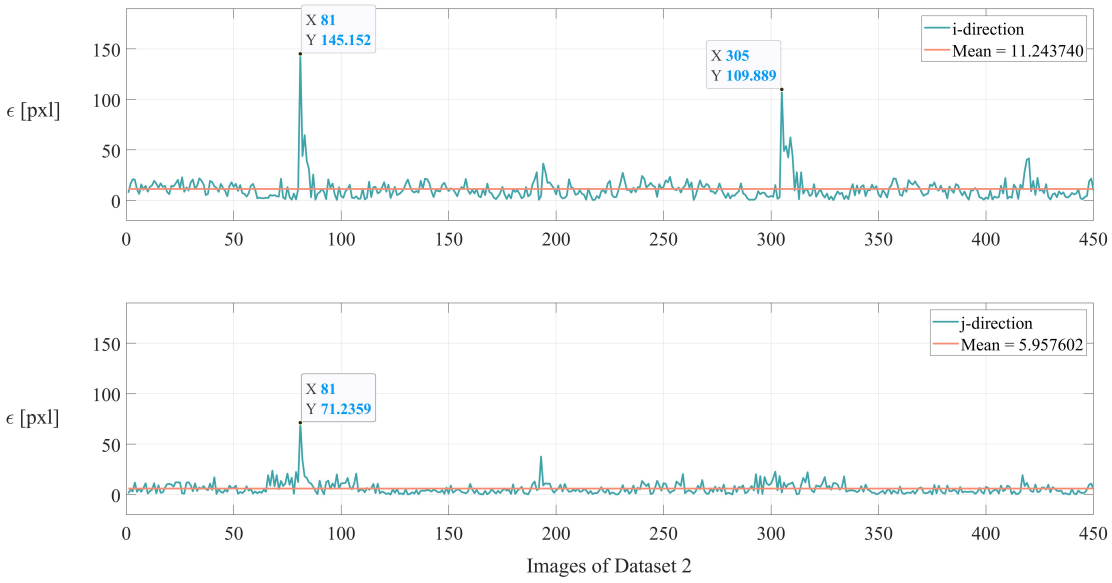

Fig. 14 ϵ_{COM} for Didymos during DCP

Fig. 14 illustrates the results of the centroiding of Didymos for the DCP testing dataset of 450 images. It is possible to see that the absolute error fluctuates around 11.24 pxl in the $i-$direction and around 5.95 pxl in the $j-$direction, with a standard deviation of $\sigma_i = 11.63\ pxl$ and $\sigma_j = 6.01\ pxl$. The error is greater in comparison to the old results shown in Table 5. This is due to the fact that, during the DCP, the distance from Didymos is reduced, resulting in a larger projection of Didymos on the images. This is also shown by looking at Fig. 14 and Fig. 5: the two peaks of the error on the $i-$direction and on the $j-$ direction of ϵ_{COM} correspond to two local minima of the range.

B. Flag Dimorphos

The performance of the IP block on the detection of Dimorphos in the images is assessed with the confusion matrix shown in Table 6. It is defined as positive class if Dimorphos is visible in the image and as negative class viceversa.

Table 6 Confusion matrix detection Dimorphos

	Actual Positive = 276	**Actual Negative** = 174
Predicted positive = 247	$TP = 246$	$FP = 1$
Predicted negative = 203	$FN = 29$	$TN = 174$

where TP, TN, FP and FN stand respectively for True Positive, True Negative, False Positive and False Negative. The confusion matrix allows to calculate the metrics to evaluate the performance of Dimorphos' recognition in the images:

- ❖ Accuracy (A): Overall accuracy of the algorithm;
- ❖ Precision (P): Out of all the predicted positive, what percentage is truly positive;
- ❖ Recall (R): Out of the all actual positive, what percentage is truly positive.

The results obtained are shown in Eq. 12, Eq. 13 and Eq. 14.

$$A = \frac{TP + TN}{TP + FP + TN + FN} = 93.3\% \tag{12}$$

$$P = \frac{TP}{TP + FP} = 99.6\% \tag{13}$$

$$R = \frac{TP}{TP + FN} = 89.4\% \tag{14}$$

The IP block is capable to identify the presence of Dimorphos with high accuracy and precision but with a medium-high recall. By lowering the cut-off value of the peak intensity of the heatmap generated by the HRNet in the regression of the COM of Dimorphos it is possible to minimize the FN and improve the recall. Neverthelesss, this might increase the FP that is important to minimize in order to limit the number of false measurements input to the navigation filter.

C. Centroiding Dimorphos

Fig. 15 illustrates the performance of the IP in estimating the position of the centroid of Dimorphos for the DCP testing subset of 247 images where Dimorphos is considered as visible by the IP. It is possible to see that the absolute error fluctuates around 17.04 pxl in the $i-$direction and around 7.8 pxl in the $j-$direction, with a standard deviation of $\sigma_i = 31.64\ pxl$ and $\sigma_j = 7.42\ pxl$. The peak of the absolute error is obtained because it represents the sole FP detected by the algorithm leading to a higher average error compared to the old results shown in Table 5.

This is the author accepted manuscript of the publication: Kaluthantrige Don, M. A., Feng, J., & Gil-Fernández, J. (2024). Convolutional-neural-network-based autonomous navigation of Hera mission around Didymos. Journal of Guidance, Control and Dynamics, 1-14. https://doi.org/10.2514/1.G008054

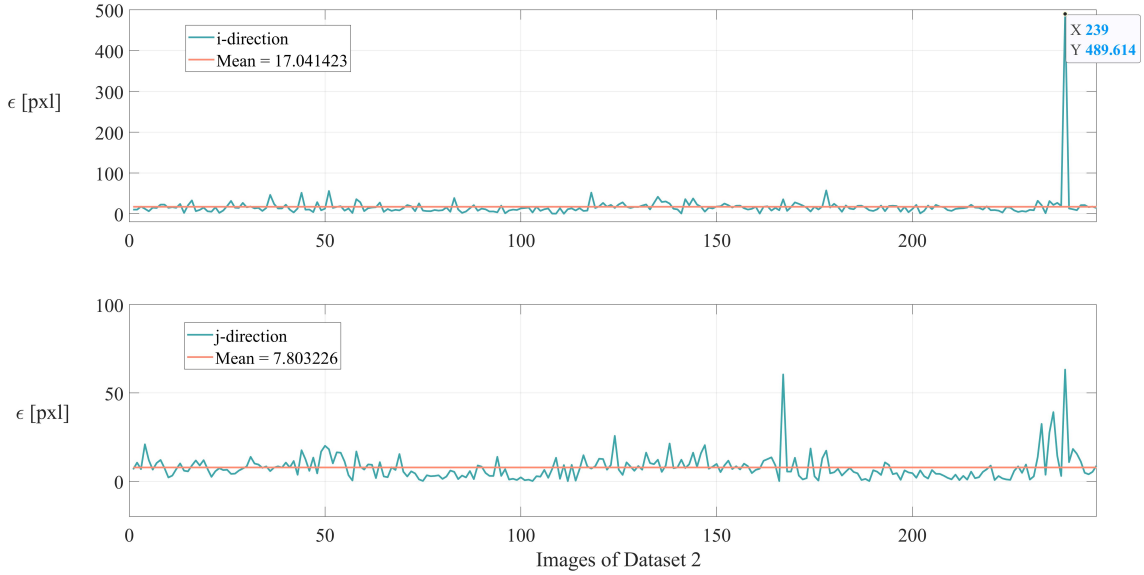

Fig. 15 ϵ_{COM} for Dimorphos during DCP

D. Range

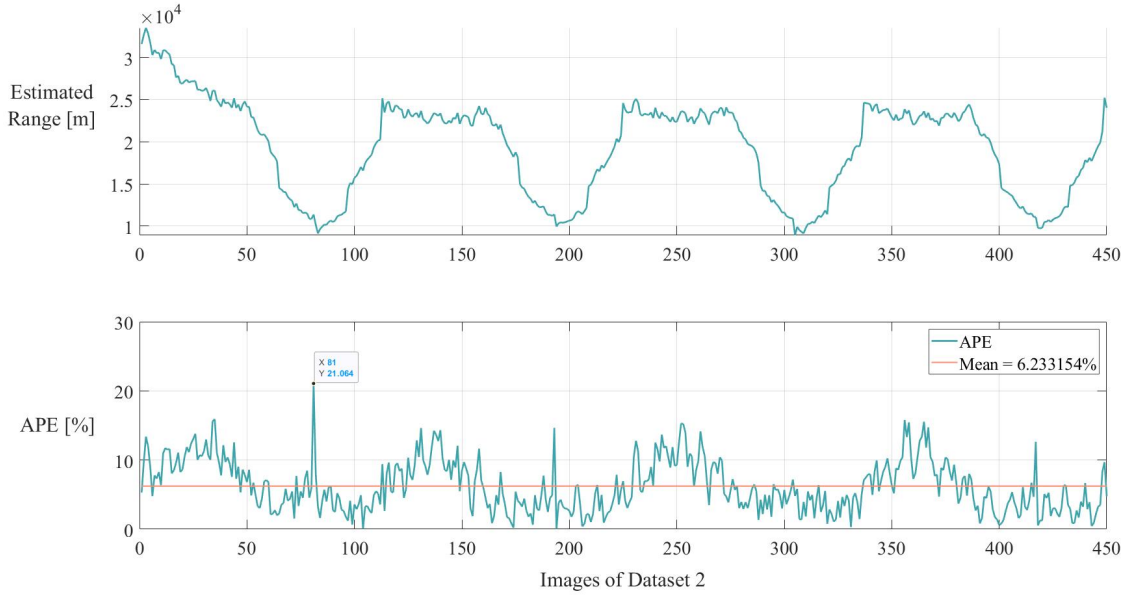

Fig. 16 Estimated range During DCP

Fig. 16 shows the estimated range attained by the IP algorithm for the DCP testing dataset. The estimation is following its GT value illustrated in Fig. 5, with an APE that oscillates around a mean value of 6.23%. The error is higher compared to the one obtained with the ECP because of the lower range of the DCP trajectory and because of the less-spherical shape of Didymos used in this work. The APE is inversely proportional to the range, due to the fact

This is the author accepted manuscript of the publication: Kaluthantrige Don, M. A., Feng, J., & Gil-Fernández, J. (2024). Convolutional-neural-network-based autonomous navigation of Hera mission around Didymos. Journal of Guidance, Control and Dynamics, 1-14. https://doi.org/10.2514/1.G008054

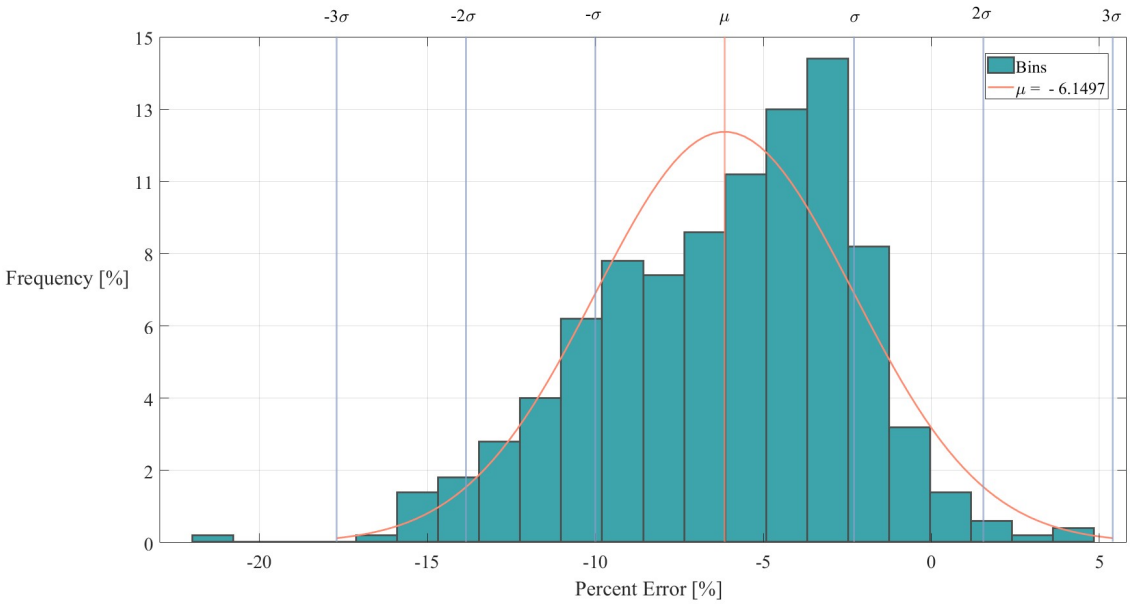

Fig. 17 Estimated range percent error distribution during DCP

that the projected image of Didymos is bigger for lower ranges. As a result, the ellipsoidal shape takes on a more prominent role, and the accuracy of approximating it as a sphere diminishes. In particular it can be seen that the peak of the APE is obtained for the same image where the ϵ_{COM} reached its peak (Fig. 14), which means that the calculated relative average distance in pixel (n_R) is inaccurate, leading to an imprecise calculation of the estimated range (Eq. 9). Nevertheless, the accuracy on the range estimation complies with the Hera mission requirements (APE $< 10\%$) [10].

Fig. 17 shows the distribution of the percent error of the estimated range obtained by the IP algorithm. The mean value is $\mu = -6.14\%$ and the standard deviation is $\sigma = 3.85\%$ which means that 68.27% of the percent error value is located between -10% and -2.29%. Ultimately, the range estimations are accurate and can be used for navigation purposes.

E. Estimated State

An error of 10 km and 0.1 m/s is introduced into each coordinate of the initial estimate of the position and velocity of the spacecraft. These errors are chosen because they are relatively high compared to the ground truth state. This allows to analyze the capacity of the measurements in correcting the estimated trajectory even in the worst navigation scenario. The complete settings of the UKF parameters are given in Table 7. The estimated trajectory resulting from the navigation filter is shown in Fig. 18, and the errors in the estimated position are shown in Fig. 19 in the TB reference frame and in Fig. 20 in the camera reference frame. Since the focus of this study is to estimate the position with centroid and range measurements, and there is no velocity measurement available, the velocity estimate is not shown since it is not affected.

This is the author accepted manuscript of the publication: Kaluthantrige Don, M. A., Feng, J., & Gil-Fernández, J. (2024). Convolutional-neural-network-based autonomous navigation of Hera mission around Didymos. Journal of Guidance, Control and Dynamics, 1-14. https://doi.org/10.2514/1.G008054

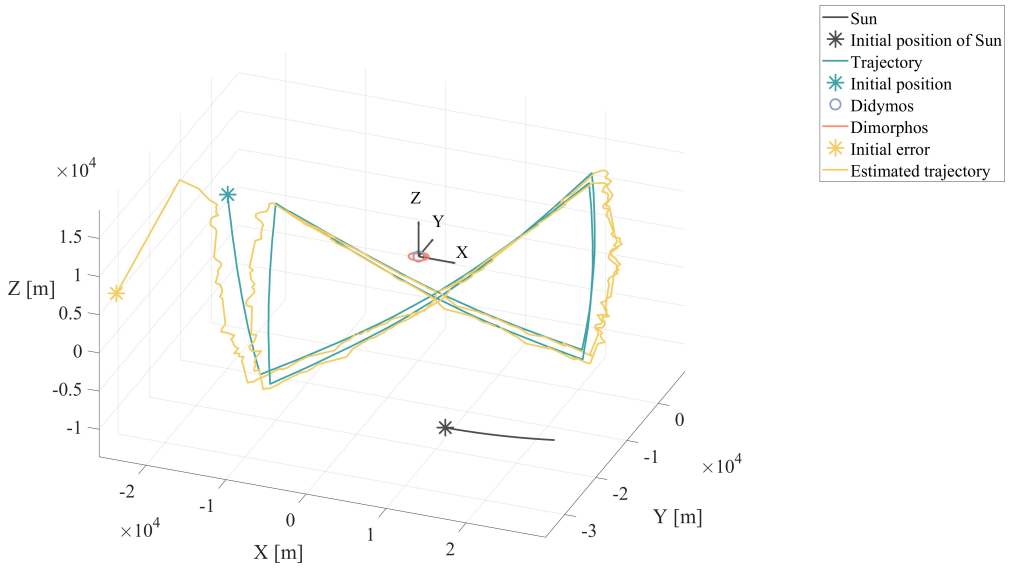

Fig. 18 Estimated trajectory vs Real Trajectory

Fig. 19 shows that initial error of 10 km in the estimated position quickly decreases after incorporating the first measurement for all the three coordinates. It can be seen that the unmodelled manoeuvres connecting each arc to the other does not affect the position error, which stays lower than 5 km for the whole trajectory. The appearances of local peaks are due to the fact that the attitude used in Eq. 9 presents some singularities given the particular relative geometry of the spacecraft/Sun/Didymos. This is shown more clearly in Fig. 20, where the peaks are mainly present only for the X and Y coordinates of the position estimation in the camera frame, which are the ones affected by the attitude. Therefore, a different relative geometry of the spacecraft with respect to the target would have a large impact on the general accuracy of the navigation system. Nevertheless, the developed navigation filter trained for the ECP is still able to perform well in a new environment and to generalize its solution.

V. Conclusion

In this work, an autonomous visual-based navigation technique with a Convolutional Neural Network (CNN)-based Image Processing (IP) algorithm is developed for the Detailed Characterization Phase (DCP) proximity operation of the Hera mission around the target binary asteroid system Didymos. The selected CNN architecture for this work is the High Resolution Network (HRNet). The algorithm is trained with synthetic images generated with Planet and Asteroid Natural scene Generation Utility (PANGU) with the previous phase of the mission i.e. the Early Characterization Phase (ECP). The shape models of Didymos and Dimorphos are updated with data collected by the Double Asteroid Redirection Test (DART) mission. The algorithm estimates the position of the centroid of Didymos and Dimorphos (if available), the range from Didymos and the associated covariances. The covariance associated with the range estimation

This is the author accepted manuscript of the publication: Kaluthantrige Don, M. A., Feng, J., & Gil-Fernández, J. (2024). Convolutional-neural-network-based autonomous navigation of Hera mission around Didymos. Journal of Guidance, Control and Dynamics, 1-14. https://doi.org/10.2514/1.G008054

Table 7 Unscented Kalman Filter variables

Variable	Symbol	Value
Initial True State	x_i	$(-1.58e4\ [m],\ -2.05e04\ [m],\ 1.5e04\ [m],$ $0.0032\ [m/s], 0.0138\ [m/s], -0.1023\ [m/s])$
Initial error in position	err_p	$(10, 10, 10)\ [km]$
Initial error in velocity	err_v	$(0.1, 0.1, 0.1)\ [m/s]$
Initial covariance matrix of the state	P	$(1000^2\ [m],\ 1000^2\ [m^2],\ 1000^2\ [m^2],\ 0.1^2$ $[m^2/s^2], 0.1^2\ [m^2/s^2], 0.1^2\ [m^2/s]^2)$
Covariance matrix of the process	Q	$(1000^2\ [m^2], 1000^2\ [m^2], 1000^2\ [m^2], 0.01^2$ $[m^2/s^2], 0.01^2\ [m^2/s^2], 0.01^2\ [m^2/s^2])$
Covariance matrix of the measurements	R	Given by the IP block

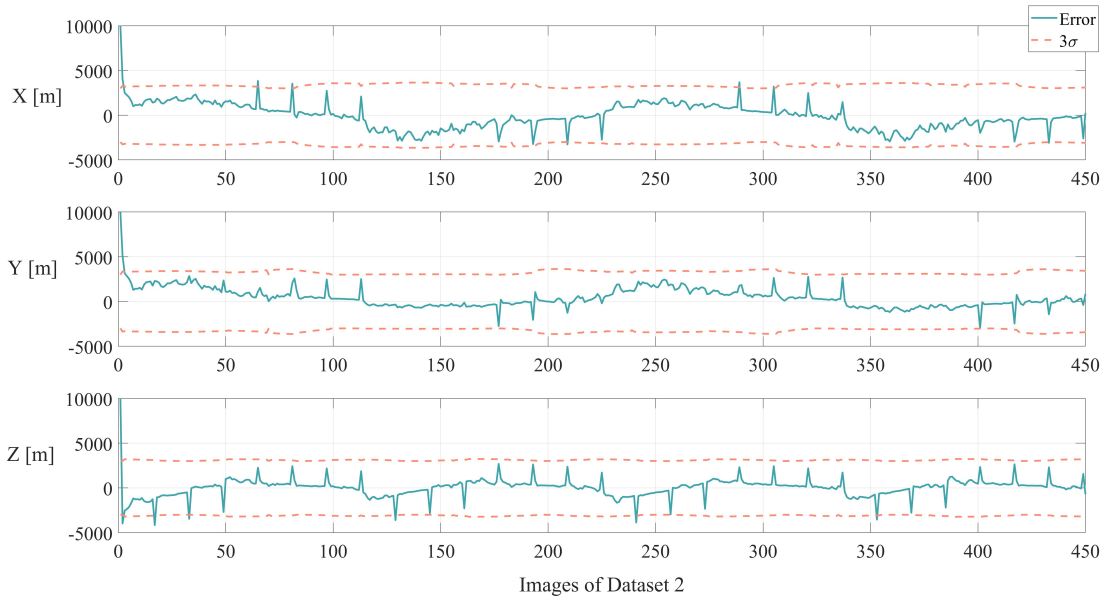

Fig. 19 Error Estimated position for Dataset 2 in the TB reference frame

is selected using the results obtained with the training process. The covariance associated with the centroids' estimation is calculated using the heatmaps generated by the HRNet. The measurements are then combined with the dynamical environment using a Unscented Kalman Filter (UKF) for the relative position estimation of the spacecraft.

The results shows that the IP algorithm solves the centroiding of Didymos and Dimorphos with high accuracy independently from the ellipsoidal shape. In particular the algorithm is able to identify whether Dimorphos is visible or not with high accuracy, precision and recall as shown from the confusion matrix represented in Table 6, which is a novelty of this work. The second main novelty is that the position of the centroid of Dimorphos is used by the UKF for the estimation of the state when available. The methodology to estimate the range is robust to the ellipsoidal shape of

This is the author accepted manuscript of the publication: Kaluthantrige Don, M. A., Feng, J., & Gil-Fernández, J. (2024). Convolutional-neural-network-based autonomous navigation of Hera mission around Didymos. Journal of Guidance, Control and Dynamics, 1-14. https://doi.org/10.2514/1.G008054

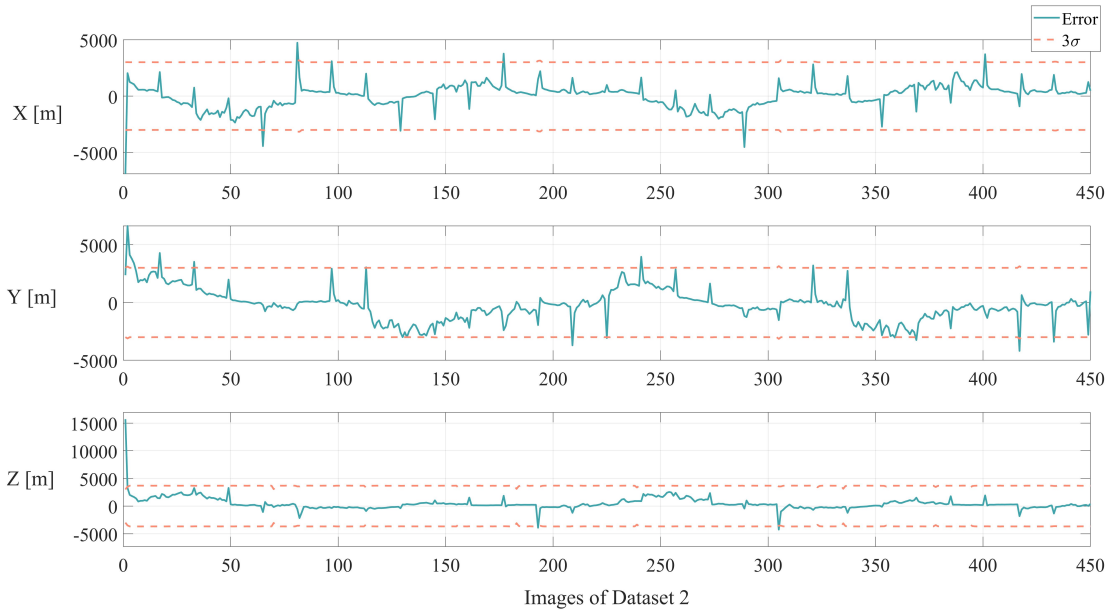

Fig. 20 Error Estimated position for Dataset 2 in the camera reference frame

Didymos, with an error higher than the one obtained in [17] where the shape model of Didymos was more spherical. Nevertheless, the Absolute Percent Error (APE) is lower than 10%, meeting the Hera mission requirements. The UKF is able to estimate the state of the spacecraft accurately. The source of the largest error are from the centroid estimation, which relies on the attitude of the camera reference frame even when it is singular.

The developed pipeline in this work enhances the robustness and autonomy of the navigation strategy for the Hera mission. Specifically, this work shows that it is possible to navigate around a binary asteroid system using only optical measurements. If higher accuracy for the state estimation is required, thermal or Light Detecting And Ranging (LIDAR) measurements can be used. It is important to point out that if the actual shape of Didymos and Dimorphos is not the same one used in this work, an offline fine-tuning of the HRNet with a subset of images taken during the ECP is necessary to estimate the position of the centroids and the range from Didymos.

Funding Sources

This study is co-funded and supported by the European Space Agency, The Netherlands under the Open Space Innovation Platform (ESA Contract No.4000133649/20/NL/MH/hm) and supported by GMV Defence and Space, Spain.

Acknowledgments

The authors would like to acknowledge the support of the Aerospace Centre of Excellence of University of Strathclyde, United Kingdom.

References

[1] Glassmeier, K. H., Boehnhardt, H., Koschny, D., Kührt, E., and Richter, I., "The Rosetta mission: Flying towards the origin of the solar system," *Space Science Reviews*, Vol. 128, No. 1-4, 2007, pp. 1–21. https://doi.org/10.1007/s11214-006-9140-8.

[2] Yoshikawa, M., Kawaguchi, J., Fujiwara, A., and Tsuchiyama, A., "Hayabusa Sample Return Mission," *Asteroids IV*, 2015, pp. 397–418. https://doi.org/10.2458/azu_uapress_9780816532131-ch021.

[3] Watanabe, S.-i., Tsuda, Y., Yoshikawa, M., Tanaka, S., Saiki, T., and Nakazawa, S., "Hayabusa2 Mission Overview," *Space Sci Rev*, 2017, pp. 3–16. https://doi.org/10.1007/s11214-017-0377-1.

[4] Lauretta, D. S., Balram-Knutson, S. S., Beshore, E., Boynton, W. V., Drouet d'Aubigny, C., DellaGiustina, D. N., Enos, H. L., Golish, D. R., Hergenrother, C. W., Howell, E. S., Bennett, C. A., Morton, E. T., Nolan, M. C., Rizk, B., Roper, H. L., Bartels, A. E., Bos, B. J., Dworkin, J. P., Highsmith, D. E., Lorenz, D. A., Lim, L. F., Mink, R., Moreau, M. C., Nuth, J. A., Reuter, D. C., Simon, A. A., Bierhaus, E. B., Bryan, B. H., Ballouz, R., Barnouin, O. S., Binzel, R. P., Bottke, W. F., Hamilton, V. E., Walsh, K. J., Chesley, S. R., Christensen, P. R., Clark, B. E., Connolly, H. C., Crombie, M. K., Daly, M. G., Emery, J. P., McCoy, T. J., McMahon, J. W., Scheeres, D. J., Messenger, S., Nakamura-Messenger, K., Righter, K., and Sandford, S. A., "OSIRIS-REx: Sample Return from Asteroid (101955) Bennu," *Space Science Reviews*, Vol. 212, No. 1-2, 2017, pp. 925–984. https://doi.org/10.1007/s11214-017-0405-1.

[5] Adams, E., Oshaughnessy, D., Reinhart, M., John, J., Congdon, E., Gallagher, D., Abel, E., Atchison, J., Fletcher, Z., Chen, M., Heistand, C., Huang, P., Smith, E., Sibol, D., Bekker, D., and Carrelli, D., "Double Asteroid Redirection Test: The Earth Strikes Back," *IEEE Aerospace Conference Proceedings*, Vol. 2019-March, 2019, pp. 1–11. https://doi.org/10.1109/AERO.2019.8742007.

[6] Michel, P., Cheng, A. F., and Küppers, M., "Asteroid Impact and Deflection Assessment (AIDA) mission: science investigaation of a binary system and mitigation test," *European Planetary Science Congress 2015, held 27 September-2 October, 2015 in Nantes, France, Online at http://meetingorganizer. copernicus. org/EPSC2015, id. EPSC2015-123*, Vol. 10, 2015, p. 123. URL http://meetingorganizer.copernicus.org/EPSC2015/EPSC2015-123.pdf.

[7] ESA Headquarters, "HERA Didymos reference model," Tech. Rep. 5, 2021.

[8] John Hopkins University Applied Physics Laboratory, "Design Reference Asteroid," Tech. Rep. 101955, 2022.

[9] Ferrari, F., Raducan, S. D., Soldini, S., and Jutzi, M., "Ejecta Formation, Early Collisional Processes, and Dynamical Evolution after the DART Impact on Dimorphos," *Planetary Science Journal*, Vol. 3, No. 7, 2022, p. 177. https://doi.org/10.3847/PSJ/ac7cf0.

[10] ESA ESTEC, "HERA : Proximity Operation Guidelines," Tech. rep., 2020.

[11] Pellacani, A., Graziano, M., Fittock, M., Gil, J., and Carnelli, I., "HERA vision based GNC and autonomy," *European Conference for AeroSpace Sciences*, 2019, pp. 1–14.

[12] Dias, N. G., Gordo, P., Onderwater, H., Melicio, R., and Amorim, A., "Analysis on the Isostatic Bipod Mounts for the HERA Mission LIDAR," *Applied Sciences (Switzerland)*, Vol. 12, No. 7, 2022. https://doi.org/10.3390/app12073497.

[13] GMV, "Mission Analysis Report," Tech. rep., 2022.

[14] Pasqualetto Cassinis, L., Menicucci, A., Gill, E., Ahrns, I., and Gil-Fernández, J., "On-Ground Validation of a CNN-based Monocular Pose Estimation System for Uncooperative Spacecraft," *8th European Conference on Space Debris*, 2021.

[15] Gil-Fernandez, J., and Ortega-Hernando, G., "Autonomous vision-based navigation for proximity operations around binary asteroids," *CEAS Space Journal*, Vol. 10, No. 2, 2018, pp. 287–294. https://doi.org/10.1007/s12567-018-0197-5.

[16] Lyzhoft, J., and Wie, B., "New image processing algorithm for terminal guidance of multiple kinetic-energy impactors for disrupting hazardous asteroids," *Astrodynamics*, Vol. 3, No. 1, 2019, pp. 45–59. https://doi.org/10.1007/s42064-018-0035-x.

[17] Kaluthantrige, A., Feng, J., and Gil-fernández, J., "CNN-based Image Processing algorithm for autonomous optical navigation of Hera mission to the binary asteroid Didymos," *Acta Astronautica*, Vol. 211, No. May, 2023, pp. 60–75. https://doi.org/10.1016/j.actaastro.2023.05.029.

[18] Pardo de Santanaya, R., and Lauer, M., "Optical measurements for rosetta navigation near the comet," *International Symposium on Space Fligth Dynamics*, 2015, pp. 1–19.

[19] Hashimoto, T., Kubota, T., Kawaguchi, J., Uo, M., Shirakawa, K., Kominato, T., and Morita, H., "Vision-based guidance, navigation, and control of Hayabusa spacecraft - Lessons learned from real operation," *IFAC Proceedings Volumes (IFAC-PapersOnline)*, Vol. 18, IFAC, 2010, pp. 259–264. https://doi.org/10.3182/20100906-5-jp-2022.00045.

[20] Saiki, T., Takei, Y., Takahashi, T., Kikuchi, S., Sawada, H., Hirose, C., Terui, F., Ogawa, N., Mimasu, Y., Ono, G., Yoshikawa, K., Takeuchi, H., Fujii, A., Masuda, T., Yasuda, S., Matsushima, K., Yoshikawa, M., Nakazawa, S., and Tsuda, Y., "Overview of Hayabusa2 Asteroid Proximity Operation Planning and Preliminary Results," *Transactions of the Japan Society for Aeronautical and Space Sciences, Aerospace Technology Japan*, Vol. 19, No. 1, 2021, pp. 52–60. https://doi.org/10.2322/tastj.19.52.

[21] Williams, B., Antreasian, P., Carranza, E., Jackman, C., Leonard, J., Nelson, D., Page, B., Stanbridge, D., Wibben, D., Williams, K., Moreau, M., Berry, K., Getzandanner, K., Liounis, A., Mashiku, A., Highsmith, D., Sutter, B., and Lauretta, D. S., "OSIRIS-REx Flight Dynamics and Navigation Design," *Space Science Reviews*, Vol. 214, No. 4, 2018. https://doi.org/10.1007/s11214-018-0501-x.

[22] Smith, E., Zhan, S., Adams, E., Chen, M., Bekker, D., Carrelli, D., Johnson, A., Heistand, C., Thomas, J., Badger, A., Rodriguez, L. M., and Tran, M. Q., "Testing Early and Often: End-to-End Testing on the Double Asteroid Redirection Test (DART)," *IEEE Aerospace Conference Proceedings*, 2020, pp. 1–9. https://doi.org/10.1109/AERO47225.2020.9172455.

[23] Agrusa, H. F., Gkolias, I., Tsiganis, K., Richardson, D. C., Meyer, A. J., Scheeres, D. J., Ćuk, M., Jacobson, S. A., Michel, P., Karatekin, Ö., Cheng, A. F., Hirabayashi, M., Zhang, Y., Fahnestock, E. G., and Davis, A. B., "The excited spin state of Dimorphos resulting from the DART impact," *Icarus*, Vol. 370, 2021. https://doi.org/10.1016/j.icarus.2021.114624.

[24] JPL, "JPL Small-Body Database Browser," , 2021. URL https://ssd.jpl.nasa.gov/sbdb.cgi?sstr=Didymos.

[25] Naidu, S. P., Benner, L. A. M., Brozovic, M., Nolan, M. C., Ostro, S. J., Margot, J. L., Giorgini, D., Hirabayashi, T., Scheeres, D. J., Pravec, P., Scheirich, P., Magri, C., and Jao, J. S., "Radar observations and a physical model of binary near-Earth asteroid 65803 Didymos , target of the DART mission," *Icarus*, Vol. 348, No. September 2019, 2020, p. 113777. https://doi.org/10.1016/j.icarus.2020.113777.

[26] ESA, "Hera Mission Instruments," , 2021. URL https://www.heramission.space/hera-instruments.

[27] Sierks, H., Keller, H. U., Jaumann, R., Michalik, H., Behnke, T., Bubenhagen, F., Büttner, I., Carsenty, U., Christensen, U., Enge, R., Fiethe, B., Gutiérrez Marqués, P., Hartwig, H., Krüger, H., Kühne, W., Maue, T., Mottola, S., Nathues, A., Reiche, K. U., Richards, M. L., Roatsch, T., Schröder, S. E., Szemerey, I., and Tschentscher, M., "The Dawn framing camera," *Space Science Reviews*, Vol. 163, No. 1-4, 2011, pp. 263–327. https://doi.org/10.1007/s11214-011-9745-4.

[28] Dunstan, M., and Martin, I., "Planet and Asteroid Natural Scene Generation Utility User Manual," Tech. Rep. 2, STAR-Dundee, 2017.

[29] Sun, K., Zhao, Y., Jiang, B., Cheng, T., Xiao, B., Liu, D., Mu, Y., Wang, X., Liu, W., and Wang, J., "High-Resolution Representations for Labeling Pixels and Regions," , 2019. URL https://arxiv.org/abs/1904.04514.

[30] Sun, K., Xiao, B., Liu, D., and Wang, J., "Deep high-resolution representation learning for human pose estimation," *Proceedings of the IEEE Computer Society Conference on Computer Vision and Pattern Recognition*, Vol. 2019-June, 2019, pp. 5686–5696. https://doi.org/10.1109/CVPR.2019.00584.

[31] Pasqualetto Cassinis, L., Fonod, R., Gill, E., Ahrns, I., and Gil-Fernández, J., "Evaluation of tightly- and loosely-coupled approaches in CNN-based pose estimation systems for uncooperative spacecraft," *Acta Astronautica*, Vol. 182, No. June 2020, 2021, pp. 189–202. URL https://doi.org/10.1016/j.actaastro.2021.01.035.

[32] Julier, S. J., and Uhlmann, J. K., "Unscented Filtering and Nonlinear Estimation," 2004, pp. 401–402.

[33] Ferrari, F., Franzese, V., Pugliatti, M., Giordano, C., and Topputo, F., "Trajectory Options for Hera ' s Milani CubeSat Around (65803) Didymos," *The Journal of the Astronautical Sciences*, 2021, pp. 973–994.

[34] Sinha, S. N., *Pan-Tilt-Zoom (PTZ) Camera*, Springer International Publishing, Cham, 2020, pp. 1–7. https://doi.org/10.1007/978-3-030-03243-2_496-1, URL https://doi.org/10.1007/978-3-030-03243-2_496-1.